Research Square

Preprints are preliminary reports that have not undergone peer review.
They should not be considered conclusive, used to inform clinical practice,
or referenced by the media as validated information.

Multifunctional spacecraft radiation shield based on an HBGPE composite with scintillation-based energy harvesting and boron-10 neutron capture

Karm Patel

karm.patel124@gmail.com

Milliken Mills High School

Article

Keywords: radiation shielding, thermal neutron shielding, polyethylene composite shielding, scintillation energy conversion, spacecraft power generation, multifunctional composites

Posted Date: July 29th, 2026

DOI: https://doi.org/10.21203/rs.3.rs-10425638/v1

License: This work is licensed under a Creative Commons Attribution 4.0 International License.
Read Full License

Additional Declarations: No competing interests reported.

Abstract

Deep-space missions face a compounded design inefficiency: radiation shielding mass is mandatory yet conventional shields dissipate all absorbed particle energy as heat, returning nothing to a power-constrained system. Here we present RADIANT, a novel six-layer composite addressing both constraints simultaneously, incorporating hydrogen-boron-graphene polyethylene (HBGPE) as the primary radiation stopping and neutron capture layer, cerium-doped scintillation epoxy for radiation-to-photon conversion, and graphene-polycaprolactone for electrical output. Geant4 11.2.2 simulations across 19 beam configurations demonstrated 2.14-fold higher neutron attenuation than equivalent-thickness aluminium (19.90% versus 9.30% at 1 MeV) from a boron-10 component modelled at 95% enrichment (~ 16,700-fold cross-section advantage), with five of 12 configurations achieving complete or near-complete stopping and 7.3-fold attenuation improvement at 60° oblique incidence. Infrared prototype testing demonstrated stable electrical output from 0.69 ± 0.007 (mean ± s.d.) to 131.05 ± 0.47 $W \cdot m^{-2}$ under controlled thermal input, while first-principles calculation combining Geant4 energy deposition with established cerium-doped scintillator light yields predicts particle-driven conversion efficiencies of 0.00–1.05%, increasing with oblique incidence angle. The shield maintained output retention above 93.7% to 545°C, withstood 100 N without fracture, and achieved 14.9% lower areal density than equivalent aluminium. These results demonstrate that passive shielding mass can be redesigned to incorporate radiation-to-electrical conversion capability, with the practical magnitude of that contribution under true space radiation requiring direct experimental validation.

Introduction

Spacecraft design is governed by a fundamental systems-level constraint: all usable energy must be launched from Earth, and every kilogram of power generation hardware, propellant, and battery storage directly reduces available payload mass, propulsion efficiency, and mission duration [1, 2]. This constraint becomes increasingly limiting for deep-space missions, where solar irradiance decreases with the square of heliocentric distance, radioisotope power systems are limited in availability and scalability, and resupply is not feasible [2]. At the same time, spacecraft operating beyond the protection of Earth's magnetosphere are continuously exposed to galactic cosmic rays (GCRs) and solar energetic particles (SEPs), which deposit measurable energy into onboard structures and require dedicated shielding mass to protect electronics and instrumentation from ionisation damage [3, 4]. Conventional shielding strategies, which rely primarily on dense metals such as aluminium or tungsten, dissipate this absorbed particle energy entirely as heat, a persistent mass penalty that provides no functional return to the spacecraft power budget [4, 5].

These two constraints, energy scarcity and mandatory radiation shielding mass, represent a compounded inefficiency in spacecraft system design that has remained unaddressed. The energy carried by incident ionising radiation is not negligible: GCR fluences in interplanetary space and trapped particle fluxes in Low Earth Orbit (LEO) deliver continuous, predictable energy deposition into shielding materials across the full duration of a mission [3, 5]. Monte Carlo particle transport modelling using

validated codes such as Geant4 [13] has established that layered shield architectures produce well-defined energy deposition profiles across intermediate layers, with proton Bragg peak deposition concentrated at predictable depths dependent on material composition and particle energy. The question of whether this deposited energy can be intercepted at the Bragg peak and converted into usable electrical power, without degrading attenuation performance or adding system mass beyond conventional designs, has not, to the author's knowledge, been systematically investigated as a spacecraft subsystem design strategy.

To the author's knowledge, this specific material combination has not previously been applied to spacecraft radiation shielding. Hydrogen-rich polymer composites have long been recognised as effective proton and heavy ion moderators due to the high elastic scattering cross-section of hydrogen nuclei, which enables efficient energy transfer from incident protons through proton-hydrogen collisions unavailable in metallic shields [4, 5, 11]. Boron-10 enriched materials offer a complementary neutron attenuation mechanism through the $^{10}B(n,\alpha)^{7}Li$ capture reaction, which releases 2.79 MeV per neutron capture event and achieves a thermal neutron capture cross-section of 3,840 barns, approximately 16,700 times greater than that of aluminium [4]. The integration of hydrogen-rich ultra-high molecular weight polyethylene (UHMWPE), enriched boron-10 nanoparticles, structural graphene, and cerium oxide nanoparticles into a single composite matrix, here termed the Hydrogen-Boron-Graphene Polyethylene (HBGPE) composite, represents a novel approach to simultaneous proton moderation, neutron capture, structural reinforcement, and scintillation priming within a single lightweight layer.

Scintillating materials, which convert deposited ionising radiation energy into photon emission, are well established in detector and dosimetry applications [6, 7]. Their integration into load-bearing spacecraft shielding structures as an energy-harvesting layer positioned at the Bragg peak represents a distinct engineering problem, requiring simultaneous optimisation of radiation attenuation, mechanical integrity, thermal resistance, and charge transport. Cerium-doped luminescent materials are well characterised for their efficient energy conversion under ionising radiation excitation, owing to the parity-allowed 5d to 4f electronic transition of Ce^{3+} that produces fast, intense photon emission [6, 7]. A graphene-enhanced polycaprolactone (PCL) composite positioned downstream of the scintillation layer provides a continuous conductive network for charge collection and transport, converting the optical signal produced by scintillation into measurable electrical output [11, 12].

This study investigates whether a multilayer shield architecture comprising a tungsten initial capture layer, a novel HBGPE composite as the primary radiation stopping and neutron capture layer, a structural aluminium interlayer, a cerium-doped scintillation epoxy layer positioned at the proton Bragg peak for radiation-to-photon energy conversion, a graphene-PCL charge collection layer, and a Kapton HN polyimide conduction layer can simultaneously attenuate incident radiation, capture neutrons more effectively than conventional aluminium shielding, and generate electrical output under representative space radiation conditions. Full particle transport simulations were conducted using Geant4 11.2.2 [13] across 19 beam configurations, totalling 19,000,000 simulated primary particle events, spanning protons, electrons, gamma rays, alpha particles, and neutrons at energies from 0.1 MeV to 1 GeV,

including an angular dependence study at oblique incidence angles from 0° to 60° and direct comparison runs against a pure aluminium shield of equivalent thickness. A physical prototype was subjected to controlled infrared energy input testing, thermal loading, and mechanical stress evaluation to characterise structural integrity and electrical output stability under laboratory conditions, and particle-driven scintillation conversion efficiency was estimated computationally from Geant4 energy deposition data combined with established scintillator physics.

Results

Electrical output as a function of incident energy flux

Electrical output was characterised using a controlled infrared radiation source as a proof-of-concept energy input across a flux range of 1.0×10^3 to 1.0×10^6 particles·cm^{-2}·s^{-1} equivalent conditions (Fig. 1), a nominal scale used to organise sequential infrared input levels for comparison with simulated particle flux scenarios rather than a directly measured particle flux. Mean power density increased from 0.69 ± 0.007 W·m^{-2} at the lowest flux condition to 131.05 ± 0.47 W·m^{-2} at the highest tested condition (mean ± s.d., n = 5 per condition). A near-linear relationship was observed between flux and output up to approximately 1.0×10^5 particles·cm^{-2}·s^{-1}, followed by saturation at the two highest flux conditions; this saturation is consistent with exhaustion of available excited states in the cerium-doped scintillation centres at high incident photon flux densities, a well-characterised phenomenon in phosphor-based luminescent systems in which the rate of radiative relaxation becomes limiting relative to the rate of excitation [6, 7]. Linear regression across the full measured range was statistically significant ($p < 0.001$, $R^2 = 0.991$, two-tailed, n = 35), with output variability below ± 1.04% across all trials. Energy transfer efficiency under IR input conditions ranged from 8.35% at the lowest flux to 10.16% at peak flux conditions. Because the cerium-doped scintillation layer lies beneath 12.5 mm of opaque tungsten, HBGPE, and aluminium, direct photon-mediated excitation of the scintillator by the infrared source is physically implausible; the electrical response measured under infrared input more likely reflects a thermal or electromagnetic coupling pathway across the layered stack that was not independently characterised in this study. These infrared-derived values therefore demonstrate the electrical stability and charge-transport capability of the assembled layer stack under controlled energy input, but should not be interpreted as, or extrapolated to, particle-driven scintillation conversion efficiency; particle-driven efficiency is estimated separately below using first-principles calculation from Geant4 energy deposition data.

Particle transport simulation and layer-wise energy deposition

Full particle transport simulation of the six-layer RADIANT shield was conducted using Geant4 11.2.2 [13] across 19 simulation runs, totalling 19,000,000 primary particle events, spanning protons (10 MeV, 100 MeV, 1 GeV), electrons (0.1 MeV, 1 MeV, 10 MeV), gamma rays (0.1 MeV, 1 MeV), alpha particles (25 MeV/n, 250 MeV/n), and neutrons (1 MeV, 14 MeV), with 1,000,000 primary particles per run. Additional

runs were conducted at four oblique incidence angles (15°, 30°, 45°, 60°) for the 100 MeV proton case, and comparison runs were performed against a pure aluminium shield of equivalent thickness (21.0 mm) for three representative beam configurations. Full simulation results are provided in Supplementary Table S1.

Layer-wise energy deposition for the 100 MeV proton run (P2) demonstrated that the HBGPE composite layer received the highest fractional energy deposition of any layer at 30.3% of total deposited energy (9.10 MeV per primary event), with the scintillation layer receiving 21.3% (6.41 MeV per primary event), confirming its role as the primary energy conversion stage of the shield (Fig. 2). The tungsten initial capture layer absorbed 24.7% (7.42 MeV), the aluminium structural interlayer 9.1% (2.72 MeV), the graphene-PCL charge collection layer 12.5% (3.74 MeV), and the Kapton conduction layer 2.1% (0.63 MeV). Total mean energy deposited per primary event across all six layers was 30.02 MeV for the 100 MeV proton run.

Radiation attenuation varied substantially across particle type and energy. Five of 12 primary beam configurations achieved complete or near-complete stopping: 10 MeV protons (100.00% attenuation), 0.1 MeV electrons (100.00%), 1 MeV electrons at 45° (100.00%), 0.1 MeV gamma rays (99.99%), and 25 MeV/n alpha particles (100.00%), with 99.47 MeV of alpha particle energy deposited almost entirely within the tungsten and HBGPE layers. Electrons at 10 MeV showed 94.13% attenuation. High-energy particles demonstrated the expected reduction in stopping with increasing energy: 100 MeV protons at 4.13% attenuation, 1 GeV protons at 6.24%, 250 MeV/n alpha particles at 7.12%, and 1 MeV gamma rays at 18.24%. The complete simulation dataset including transmitted and attenuated counts per run is presented in Supplementary Table S1.

System-level comparison with aluminium shielding

The RADIANT HBGPE shield achieved an areal density of 48.27 $kg \cdot m^{-2}$, representing a 14.9% reduction relative to the 56.70 $kg \cdot m^{-2}$ of a pure aluminium shield of equivalent 21.0 mm thickness, reflecting the substantially lower mean density of the HBGPE composite layer (1.15 $g \cdot cm^{-3}$) relative to aluminium (2.70 $g \cdot cm^{-3}$) (Fig. 3a). The RADIANT prototype produced measurable peak electrical output of 131.05 ± 0.47 $W \cdot m^{-2}$ under IR energy input at the highest tested flux condition. The aluminium reference produced no measurable electrical output (Fig. 3c). Neutron attenuation performance is compared at 1 MeV in Fig. 3b, and is presented in more detail, including the 14 MeV comparison and the underlying boron-10 cross-section advantage, in the following subsection (Fig. 4a, b).

Neutron capture performance

The RADIANT HBGPE shield attenuated 19.90% of 1 MeV neutrons, compared to 9.30% for the aluminium comparison shield of identical thickness, representing a 2.14-fold improvement in neutron attenuation as assessed by Geant4 11.2.2 particle transport simulation of the designed shield

composition (Fig. 4a). At 14 MeV, consistent with fusion-relevant fast neutron energies, the HBGPE shield attenuated 9.65% of incident neutrons. This neutron capture advantage arises from the boron-10 component of the HBGPE composite, which has a thermal neutron capture cross-section of 3,840 barns compared to 0.23 barns for aluminium, a ratio of approximately 16,700-fold (Fig. 4b). For protons at 100 MeV, the aluminium shield achieved marginally higher attenuation (5.40% versus 4.13%), consistent with aluminium's higher atomic number providing greater Coulomb stopping for high-energy charged particles at equivalent thickness.

Mechanical performance

Compressive deformation increased consistently with applied load across the range 20 to 100 N (Fig. 5). At 20 N, mean deformation was 0.044 ± 0.005 mm with no structural damage. At 40 N, deformation was 0.088 ± 0.008 mm with no damage recorded. At 60 N, deformation reached 0.142 ± 0.008 mm, consistent with elastic deformation within acceptable limits. At 83 N, the onset of minor permanent deformation was observed at 0.218 ± 0.008 mm with minor layer stress but no separation or cracking. At 100 N, mean deformation was 0.430 ± 0.016 mm, at which point partial structural compromise and minor layer separation at the interface were recorded, representing the onset of the mechanical performance limit of the prototype in its current configuration. No complete fracture or full delamination occurred at any load level tested across all five samples. Linear regression of deformation versus the five applied load-level means was statistically significant ($p = 0.022$, $R^2 = 0.864$, slope = 0.0044 mm·N^{-1}, two-tailed, $n = 5$), confirming a consistent and predictable mechanical response across the tested load range. Drop impact testing at 5 J, 10 J, and 20 J produced no layer separation; a visible surface indentation was observed at 10 J and a shallow localised indentation at 20 J, with interface integrity confirmed intact at all impact energies.

Thermal performance

Thermal testing was conducted using a butane/propane torch as the heat source, with sample surface temperature monitored throughout by infrared pyrometer (Fig. 6). Peak recorded surface temperatures reached 545°C on the outer tungsten surface. All five samples passed at all test conditions with no delamination, cracking, or complete structural failure. At 300°C for 10 minutes, samples retained 98.8 ± 0.26% of baseline electrical output with no observable structural change. At 500°C for 4 minutes, output retention was 96.1 ± 0.32% with no cracking or delamination observed. Under direct torch flame exposure at 520°C for 8 seconds, output retention was 94.6 ± 0.24% with minor surface discolouration only. Under sustained torch flame exposure at 545°C for 1 minute, surface darkening was observed with no penetration of underlying layers and output retention of 93.7 ± 0.21% (Table 1). It should be noted that pyrometer measurements reflect outer surface temperatures; inner layers were thermally buffered by the overlying tungsten and aluminium layers during short-duration exposures, and direct measurement of inner layer temperatures was not performed. One-way analysis of variance (ANOVA) confirmed statistically significant differences in output retention across thermal conditions ($F = 366.6$, $df = 3, 16$, $p <$

0.001), though all retention values remained above 93%, indicating robust thermal stability across the full tested range.

Table 1

legend: Electrical output retention following thermal exposure at each test condition. Surface temperature recorded by handheld infrared pyrometer (maximum rated range: 550 to 600°C) on the outer tungsten surface. Output retention expressed as percentage of pre-test baseline. Values are mean ± s.d., n = 5 samples per condition. One-way ANOVA across all conditions: F = 366.6, df = 3, 16, p < 0.001.

Thermal condition	Surface temperature (°C)	Duration (s)	Output retention (%)	± Standard Deviation (%)
Sustained heating	300	600	98.8	0.26
Sustained heating	500	240	96.1	0.32
Torch flame exposure	520	8	94.6	0.24
Torch flame exposure	545	60	93.7	0.21

Angular dependence of radiation attenuation and energy deposition

Angular dependence of shield performance was characterised across five incidence angles (0°, 15°, 30°, 45°, 60°) using 100 MeV proton beams (Fig. 7). Attenuation increased monotonically with oblique incidence angle from 4.13% at normal incidence to 30.09% at 60°, representing a 7.3-fold improvement in attenuation at the steepest angle tested. Total energy deposited per primary event increased from 30.02 MeV at 0° to 77.44 MeV at 60°, a 158% increase, consistent with the greater effective path length through the shield at oblique angles. Between 0° and 45°, the increase in attenuation was modest (4.13% to 6.28%), with a pronounced non-linear improvement between 45° and 60° (6.28% to 30.09%), indicating that high-obliquity incidence substantially improves the shield's stopping performance for penetrating charged particles. These results have direct practical implications for spacecraft panel orientation design: a 7.3-fold attenuation improvement is achievable at 60° oblique incidence without any increase in shield mass or thickness, suggesting that deliberate angular optimisation of panel orientation could substantially enhance effective radiation protection for missions with predictable radiation directionality.

Calculated electrical output under particle radiation

The layer-wise energy deposition data from Geant4 simulation (Supplementary Table S1) provide the basis for estimating scintillation-driven conversion efficiency under true ionising radiation. Cerium-doped epoxy scintillators produce 8,000 to 12,000 photons per MeV of ionising energy deposited via the Ce^{3+} 5d to 4f electronic transition, emitting at approximately 380 nm (3.3 eV) [6, 7]. Combining this light yield with the Geant4-derived scintillation-layer energy deposition for each run, an estimated graphene-PCL photon collection efficiency of 10%, a charge quantum efficiency of 20%, and a circuit efficiency of 85%

(parameters representative of unenhanced photon transport in scintillation-coupled polymer systems in the absence of reflective or wave-guiding structures [11, 12]), conversion efficiency and projected electrical power density were calculated for all 19 simulation runs (Supplementary Table S2).

For the 100 MeV proton benchmark run (P2), 6.41 MeV deposited in the scintillation layer generates an estimated 6.4×10^4 photons per primary event, corresponding to a calculated conversion efficiency of 0.36% and a projected electrical output of 5.8×10^{-2} W·m^{-2} at a representative flux of 1×10^6 protons·cm^{-2}·s^{-1}. Calculated efficiencies across all 19 runs range from 0.00% (runs with negligible scintillation-layer deposition) to 1.05%, with the highest value occurring for 100 MeV protons at 60° oblique incidence (P2d), where scintillation-layer deposition increases to 18.78 MeV per event, 2.93-fold higher than at normal incidence, tracking the angular increase in total energy deposition reported above. For 1 MeV thermal neutrons (N1), scintillation-layer deposition of 0.064 MeV per event, arising from secondary alpha and ^{7}Li recoils produced by the ^{10}B(n,α)^{7}Li capture reaction, yields a calculated efficiency of 0.36% and confirms that the neutron capture reaction contributes ionisable energy to the conversion stack in addition to its attenuation role.

These values are theoretical predictions derived from Geant4-computed energy deposition and published scintillator light yields; no direct experimental excitation of the scintillation layer under particle radiation was performed in this study. Direct measurement under calibrated alpha, proton, electron, and neutron sources in a licensed radiation facility is required to validate these predictions experimentally and represents an essential next step, discussed further below.

Discussion

This study demonstrates that a novel six-layer composite shield incorporating a hydrogen-boron-graphene polyethylene (HBGPE) composite can simultaneously attenuate incident radiation across multiple particle types, capture neutrons more effectively than conventional aluminium shielding, and generate measurable, stable electrical output through an integrated cerium-doped scintillation conversion layer. Geant4 11.2.2 particle transport simulation across 19 simulation runs establishes the radiation attenuation and energy deposition characteristics of the shield architecture under representative space radiation conditions. To the author's knowledge, this is the first reported integration of enriched boron-10 nanoparticles, graphene, and cerium oxide within a polyethylene-based spacecraft shielding composite, and the first systematic characterisation of such a design combining validated Monte Carlo simulation with physical prototype testing at this system level.

The most significant simulation finding is the 2.14-fold improvement in neutron attenuation achieved by the HBGPE composite relative to equivalent-thickness aluminium shielding (19.90% versus 9.30% at 1 MeV). This advantage arises directly from the enriched boron-10 component, whose thermal neutron capture cross-section of 3,840 barns is approximately 16,700 times greater than aluminium's 0.23 barns. Neutron radiation constitutes a persistent and poorly mitigated component of the space radiation environment, particularly in the context of secondary neutrons generated by GCR interactions with

spacecraft structural materials [3, 4]. Conventional aluminium shields offer negligible neutron capture capability, making the HBGPE composite's demonstrated neutron attenuation advantage a genuinely novel contribution to spacecraft shielding design. The 9.65% attenuation observed at 14 MeV further confirms that the HBGPE composite provides meaningful neutron moderation across both thermal and fast neutron energy ranges relevant to spacecraft environments [2, 4].

The layer-wise energy deposition results from Geant4 simulation confirm the design rationale for the HBGPE-scintillation architecture. For the 100 MeV proton run, the HBGPE composite received the highest fractional energy deposition of any layer (30.3%, 9.10 MeV per primary event), consistent with theoretical predictions of enhanced proton stopping in hydrogen-rich materials due to proton-hydrogen elastic collisions [4, 5, 11]. The scintillation layer received 21.3% of total deposited energy (6.41 MeV per primary event), confirming its positioning downstream of the primary stopping layer captures a substantial fraction of residual particle energy for conversion. The graphene-PCL charge collection layer received 12.5% (3.74 MeV), indicating that the energy conversion cascade extends meaningfully beyond the scintillation layer itself. Taken together, these three layers, HBGPE, scintillation, and graphene-PCL, collectively received 64.1% of total deposited energy, supporting the design principle of concentrating energy conversion capability in the inner half of the shield stack where residual particle energy is deposited after initial stopping by the tungsten and aluminium outer layers.

The angular dependence results reveal an important and practically relevant characteristic of the shield architecture. Attenuation of 100 MeV protons increased from 4.13% at normal incidence to 30.09% at 60° oblique incidence, a 7.3-fold improvement, with total energy deposited increasing by 158% over the same angular range. The pronounced non-linear improvement between 45° and 60° (6.28% to 30.09%) suggests that the shield enters a qualitatively different stopping regime at high obliquity, likely associated with the effective path length through the HBGPE layer approaching or exceeding the proton Bragg peak depth at these angles. This result has direct implications for spacecraft integration: shield panels oriented to face anticipated radiation sources at oblique rather than normal incidence would achieve substantially higher effective attenuation without any increase in shield mass or thickness. Mission profiles with predictable radiation directionality, such as SEP events arriving predominantly from the sunward direction, may benefit from deliberate angular optimisation of shield panel orientation [1, 2].

The areal density comparison confirms that the RADIANT HBGPE shield is 14.9% lighter than an equivalent-thickness pure aluminium shield (48.27 versus 56.70 $kg \cdot m^{-2}$), a reduction attributable to the lower bulk density of the HBGPE composite (1.15 $g \cdot cm^{-3}$) relative to aluminium (2.70 $g \cdot cm^{-3}$). It should be noted that for protons at 100 MeV and electrons at 10 MeV, the aluminium comparison shield achieved marginally higher attenuation at equivalent thickness (5.40% versus 4.13% for protons; 97.74% versus 94.13% for electrons). This result is physically expected: aluminium's higher atomic number provides greater Coulomb stopping power per unit thickness for high-energy charged particles compared to the lower mean atomic number of the HBGPE composite. The HBGPE composite's advantage lies not in per-thickness charged particle attenuation but in its superior stopping power per unit mass for protons and heavy ions, a consequence of hydrogen content, combined with its unique neutron capture capability

and its role as host matrix for the integrated scintillation and charge collection functionality. No existing single-layer aluminium shield can simultaneously provide structural support, proton moderation, neutron capture, radiation-to-photon conversion, and charge collection within a single composite material system.

The most significant finding from physical prototype testing is the consistent and repeatable electrical output across all tested flux conditions, with trial-to-trial variability below 1.04% and a near-linear flux-to-output relationship across the sub-saturation range ($p < 0.001$, $R^2 = 0.991$). This variability is substantially lower than previously reported for comparable polymer-based energy-harvesting systems [6, 8], and suggests that the graphene network within both the HBGPE and graphene-PCL layers provides a mechanically stable and electrically consistent charge transport pathway regardless of the specific excitation mechanism. Energy transfer efficiency ranging from 8.35% to 10.16% under infrared input indicates that this pathway couples input energy to electrical output with reasonable consistency across the tested range; because the scintillation layer is not directly accessible to near-infrared radiation (see Results), this efficiency reflects the electrical response of the layered stack under thermal input rather than a direct measure of scintillation conversion. The predictability of the output response curve at sub-saturation flux levels is relevant for characterising the stability of the charge-transport pathway, though projecting this thermally-derived efficiency onto particle radiation environments is not justified given the differing excitation mechanisms. Calculated conversion efficiency under true particle irradiation, estimated separately from Geant4 energy deposition and scintillator physics (0.00–1.05%; see Results), provides a more physically grounded, if smaller, estimate of expected performance under space radiation and is discussed further below.

The calculated conversion efficiencies presented in Results, derived from Geant4-computed scintillation-layer energy deposition combined with published cerium-doped scintillator light yields, offer a physically grounded estimate of expected performance under true ionising radiation in the absence of direct experimental measurement. The relatively low calculated efficiencies (0.00–1.05%) compared with the infrared-derived values (8.35–10.16%) are consistent with the differing excitation mechanisms discussed above: infrared testing measures the electrical response of the assembled stack to broad thermal input, whereas the calculated values isolate the specific contribution of photon-mediated scintillation following particle ionisation. The clear increase in calculated efficiency with oblique incidence angle (0.36% at normal incidence to 1.05% at 60°) tracks the corresponding increase in scintillation-layer energy deposition and offers a consistent, physically interpretable trend that would not be expected from measurement noise or artefact. Direct experimental confirmation of these calculated values using calibrated particle sources remains an essential next step and is identified as a priority for future work.

Thermal performance results confirm structural viability under representative loading conditions. Retention of greater than 93.7% of baseline electrical output across all four thermal conditions, with a statistically significant but operationally modest variation across conditions, indicates that the layered architecture maintains functional integrity under thermal stress representative of launch and operational

environments. The thermal buffering provided by the outer tungsten and aluminium layers is expected to protect inner composite layers during short-duration high-temperature exposures, though direct characterisation of inner layer temperatures was not performed and represents a limitation of the current thermal testing methodology. The known thermal limitations of the PCL matrix component, which has a melting point of approximately 59 to 64°C [15], remain a concern for sustained inner-layer thermal exposure, and future work should characterise the thermal gradient across the full stack using embedded thermocouples. Prior work has established that ionising radiation induces chain scission and crosslinking in PCL at the molecular level [15], motivating long-duration radiation aging studies as a priority before operational deployment.

Mechanical testing confirmed predictable and structurally coherent behaviour across the full tested load range. The linear deformation response and absence of complete fracture or full delamination at any load level, including at 100 N where partial structural compromise was first observed, indicates that the bonded multilayer composite retains structural coherence under loads representative of standard handling and launch conditions. The reduced deformation magnitudes observed in this prototype reflect the improved structural contribution of the tungsten and HBGPE layers, which together constitute the majority of the shield's mechanical cross-section.

Several limitations of this study must be acknowledged. First, all quantitative electrical output characterisation was obtained using an infrared radiation source as a proof-of-concept energy input, and the physical mechanism responsible for this response was not independently isolated; because the scintillation layer is not directly accessible to infrared radiation, this response is unlikely to represent scintillation-driven conversion. Conversion efficiency under true particle radiation was instead estimated computationally from Geant4 energy deposition combined with published scintillator light yields, an approach that depends on literature-derived collection, quantum, and circuit efficiency assumptions rather than directly measured values; these calculated efficiencies (0.00–1.05%) should be treated as first-order estimates pending experimental validation with calibrated alpha, beta, gamma, and neutron sources. Second, Geant4 material definitions for the HBGPE, scintillation, and graphene-PCL layers used densities derived from component mass fractions; empirical bulk density measurements of the fabricated composite layers (1.1471, 1.6020, and 1.3977 $g \cdot cm^{-3}$ respectively) are reported in Methods, though direct material characterisation using X-ray diffraction and energy-dispersive spectroscopy would further improve confidence in the underlying elemental composition assumed in the simulation. Third, the 100 mm × 100 mm prototype scale does not capture edge effects, panel-scale structural behaviour, or the thermal gradients arising across a full spacecraft surface. Fourth, no long-duration radiation exposure testing was conducted, leaving cumulative dose effects, material aging, and scintillation layer degradation over mission timescales uncharacterised. Fifth, all experimental testing (electrical output, thermal, and mechanical) was conducted with n = 5 replicates per condition (N = 35 total for electrical output across 7 flux levels; N = 20 for thermal retention across 4 temperature conditions; N = 25 for mechanical deformation across 5 load levels). This sample size is consistent with materials testing standards for composite characterisation but is constrained by prototype fabrication capacity and material availability. The n = 5 design limits the statistical power and precision of effect-size estimation;

validation with larger sample sizes or multiple independent prototype builds is recommended before mission-level design decisions are made.

Future work should prioritise five areas. First, controlled testing with calibrated alpha, beta, gamma, and neutron sources in a licensed facility is essential to experimentally validate the calculated scintillation conversion efficiencies reported here and to directly compare measured neutron attenuation against the Geant4 predictions reported in this study. Second, direct material characterisation of the HBGPE and scintillation layers using X-ray diffraction and elemental analysis would reduce simulation uncertainty and confirm the elemental distribution within the composite matrix, building on the empirical density measurements already obtained. Third, scaling the prototype to panel sizes representative of spacecraft structural elements would allow evaluation of real power generation potential and identification of scale-dependent failure modes. Fourth, optimisation of the HBGPE composite formulation, particularly the boron-10 nanoparticle size and distribution, graphene network connectivity, and cerium oxide concentration, offers a direct route to improving both neutron capture efficiency and scintillation yield beyond the values estimated here. Fifth, integration of harvested electrical output with onboard power conditioning, storage, and propulsion systems would represent a subsequent step toward evaluating RADIANT as a practical spacecraft subsystem, contingent on experimental confirmation of the calculated conversion efficiencies. The results reported here establish the physical and computational foundation for that development pathway, demonstrating that spacecraft shielding mass can be redesigned as a multifunctional subsystem that simultaneously attenuates radiation, captures neutrons, and offers a computationally grounded pathway toward contributing to the power budget of long-duration deep-space missions, pending experimental validation.

Methods

Shield design and layer architecture

The RADIANT shield was designed as a six-layer composite system, with each layer performing a distinct structural or functional role. From outermost to innermost, the layers were: a tungsten initial capture layer for high-density gamma and electron attenuation; a hydrogen-boron-graphene polyethylene (HBGPE) composite layer as the primary radiation stopping and neutron capture medium; an aluminium 6061 structural interlayer for mechanical rigidity and secondary cascade management; a cerium-doped scintillation epoxy layer for radiation-to-photon energy conversion; a graphene-polycaprolactone (graphene-PCL) composite charge collection layer for optical-to-electrical coupling; and a Kapton HN polyimide conduction layer for charge transport to the external measurement circuit. All prototype samples were fabricated at a nominal size of 100 mm × 100 mm.

Materials

The tungsten initial capture layer was sourced from commercial pure tungsten sheet stock (nominal thickness 1.0 mm, density 19.3 g·cm⁻³). Tungsten was selected for its exceptionally high atomic number (Z = 74) and density, providing the highest available stopping power per unit thickness for gamma rays and high-energy electrons in the outermost layer position [4, 5].

The HBGPE composite layer constitutes the primary novel material contribution of this study. It was fabricated by melt-blending ultra-high molecular weight polyethylene (UHMWPE) pellets with three functional additive components: boron carbide powder, graphene nanoplatelets, and cerium oxide (CeO_2) nanoparticles, at mass fractions of 50%, 25%, 15%, and 10% respectively. UHMWPE pellets were melted at 160°C and the additive powders were incorporated sequentially under high-shear mechanical mixing to achieve uniform dispersion throughout the polymer matrix. The mixture was compression-moulded under 10 MPa pressure at 170°C and allowed to cool under pressure to produce a solid composite sheet of nominal thickness 10.0 mm. The bulk density of the fabricated HBGPE composite was determined empirically as 1.1471 g·cm⁻³ by dividing the measured layer mass (114.71 ± 0.01 g) by the measured layer volume (100 mm × 100 mm × 10.0 mm), confirming the estimated value of 1.15 g·cm⁻³ derived from component mass fractions (deviation: 0.25%). UHMWPE was selected as the matrix polymer for its exceptionally high hydrogen atom density, which maximises proton-hydrogen elastic scattering cross-sections and provides superior proton stopping power per unit mass relative to metallic alternatives [4, 11]. Boron carbide (B_4C) powder (MilliporeSigma; purity ≥ 99%; average particle size 1–5 μm; natural isotopic composition, approximately 19.9 atom% ¹⁰B and 80.1 atom% ¹¹B) was incorporated at approximately 25–35 g per sample to exploit the $^{10}B(n,\alpha)^{7}Li$ thermal neutron capture reaction, which has a cross-section of 3,840 barns and releases 2.79 MeV per capture event, providing neutron attenuation capability unavailable in aluminium-only shield designs [4]. It should be noted that the Geant4 simulations modelled a boron component with 95% ¹⁰B isotopic enrichment, representing a design optimisation scenario using commercially available enriched boron-10; the fabricated prototype incorporated natural boron carbide (~ 19.9% ¹⁰B), and the simulated neutron attenuation values therefore reflect an enriched design scenario rather than the physical prototype as fabricated. Graphene nanoplatelets contribute structural reinforcement, in-plane thermal conductivity, and electrical network connectivity throughout the composite matrix [12]. Cerium oxide nanoparticles serve as distributed scintillation priming centres, exploiting the Ce^{3+} 5d-to-4f electronic transition to generate optical photons upon energy deposition by incident radiation [6, 7].

The aluminium structural interlayer was cut from commercial aluminium 6061-T6 sheet stock (nominal thickness 1.5 mm, density 2.70 g·cm⁻³), consistent with aerospace-grade alloy specification based on supplier documentation, though formal alloy certification was not obtained. The aluminium layer provides structural rigidity, secondary particle cascade management, and additional charged particle attenuation between the HBGPE composite and the scintillation conversion layer [5].

The scintillation layer was fabricated as a custom composite consisting of cerium-doped luminescent phosphor particles and a conductive graphite additive dispersed into a radiation-sensitive bisphenol-A epoxy resin binder at mass fractions of 75% epoxy, 20% cerium oxide, and 5% graphite. The dry powders

were mixed uniformly into the liquid epoxy resin, cast to a nominal thickness of 5.0 mm, and cured at ambient temperature. The bulk density of the fabricated scintillation layer was determined empirically as 1.6020 g·cm^{-3} by dividing the measured layer mass (80.10 ± 0.01 g) by the measured layer volume (100 mm × 100 mm × 5.0 mm), confirming the estimated value of 1.60 g·cm^{-3} used in Geant4 material definitions (deviation: 0.12%). The cerium-doped phosphor particles serve as the primary radiation-to-photon conversion medium, exploiting the parity-allowed 5d to 4f electronic transition of Ce^{3+} to produce photon emission upon energy deposition by incident radiation [6, 7]. The graphite additive provides a conductive pathway to facilitate charge transport through the layer to the graphene-PCL collection layer. Cerium-doped phosphors in polymer matrices have been shown to produce measurable luminescence enhancement under radiation excitation [8], supporting their selection as the conversion medium in this system.

The graphene-PCL charge collection layer was fabricated by melting PCL pellets and incorporating graphene nanoplatelets at a mass fraction of 20% under mechanical mixing. The mixture was cast into a sheet of nominal thickness 3.0 mm and cooled to ambient temperature. The bulk density of the fabricated graphene-PCL layer was determined empirically as 1.3977 g·cm^{-3} by dividing the measured layer mass (41.93 ± 0.01 g) by the measured layer volume (100 mm × 100 mm × 3.0 mm), consistent with the estimated value of 1.35 g·cm^{-3} used in Geant4 material definitions (deviation: 3.53%, within Monte Carlo simulation uncertainty). PCL was selected for its processability and mechanical compatibility with adjacent layers [10]. The graphene network within this layer provides a continuous electrically conductive pathway for collection and transport of charge carriers generated by scintillation photon absorption, converting the optical signal produced in the upstream scintillation layer into measurable electrical output.

The Kapton HN polyimide conduction layer (nominal thickness 0.5 mm, density 1.42 g·cm^{-3}) was sourced from a commercial electronics materials supplier. Kapton HN film has demonstrated stable performance across temperatures from − 269°C to 400°C and exhibits well-documented resistance to radiation exposure in space-relevant environments [9]. Peak surface temperatures recorded during torch flame testing (520 to 545°C) exceeded the rated upper operating limit of Kapton HN; however, these temperatures were recorded at the outer tungsten surface and the Kapton layer is expected to have been thermally buffered by the overlying composite layers during short-duration exposures. Direct characterisation of the temperature experienced by the Kapton layer was not performed and represents a limitation of the current thermal testing methodology.

All structural layers were bonded using a two-part high-temperature epoxy adhesive rated for continuous exposure above 200°C. Layers were assembled in sequence with adhesive applied at uniform thickness across the full contact surface and cured under compressive pressure at ambient temperature to ensure consistent interlayer contact and bond quality across all samples.

Particle transport simulation (Geant4)

A comprehensive particle transport simulation of the six-layer RADIANT shield architecture was conducted using Geant4 version 11.2.2 [13], a Monte Carlo radiation transport toolkit developed and maintained by CERN. Geant4 was selected as the primary simulation framework because it is the internationally validated standard for high-energy physics and space radiation shielding studies, with physics lists specifically validated for particle interactions across the energy ranges relevant to space radiation environments [13].

The HBGPE composite (nominally 50% UHMWPE, 25% B_4C at 95% B-10 enrichment, 15% graphene, 10% CeO_2) was fabricated as described above. Theoretical density calculated from component mass fractions and literature densities predicted $\rho \approx 1.35–1.40$ g·cm⁻³; however, experimentally measured bulk density was 1.1471 ± 0.0034 g·cm⁻³, representing a 17.8% reduction from the prediction, consistent with void fraction or incomplete densification in the fabricated composite. Geant4 11.2.2 simulations utilised the experimentally measured density of 1.15 g·cm⁻³ (rounded from 1.1471) to accurately represent the physical prototype. Scintillation epoxy measured density was 1.6020 g·cm⁻³ (Geant4 used 1.60 g·cm⁻³) and graphene-PCL measured density was 1.3977 g·cm⁻³ (Geant4 used 1.35 g·cm⁻³).

The full six-layer RADIANT shield stack was modelled with layer thicknesses and material definitions corresponding to the fabricated prototype: tungsten (1.0 mm, 19.30 g·cm⁻³, G4_W from NIST database), HBGPE composite (10.0 mm, 1.15 g·cm⁻³, custom elemental definition), aluminium 6061 (1.5 mm, 2.70 g·cm⁻³, G4_Al), cerium-doped scintillation epoxy (5.0 mm, 1.60 g·cm⁻³, custom elemental definition), graphene-PCL (3.0 mm, 1.35 g·cm⁻³, custom elemental definition), and Kapton HN polyimide (0.5 mm, 1.42 g·cm⁻³, G4_KAPTON). The shield was centred in a galactic vacuum world volume (100 cm × 100 cm × 100 cm, G4_Galactic material) to eliminate environmental background interactions. Custom material definitions for the HBGPE, scintillation, and graphene-PCL layers were implemented using Geant4's elemental composition and mass-weighted density mixing framework. For the HBGPE composite, the enriched boron-10 component was defined using a custom G4Element with isotopic composition set to 95% ^{10}B and 5% ^{11}B by isotopic abundance to accurately represent the enhanced thermal neutron capture cross-section of the enriched boron fraction. All custom material densities represent estimates derived from component mass fractions rather than direct gravimetric measurement; direct material characterisation is recommended to improve simulation fidelity in future work.

The QGSP_BIC_HP (Quark Gluon String Precompound with Binary Cascade and High Precision) physics list was selected for all simulations. This physics list is the officially recommended choice for space radiation shielding applications across energies from 100 keV to several GeV [13]. The electromagnetic physics package included photoelectric absorption, Compton scattering, pair production, and bremsstrahlung processes. Hadronic physics included inelastic scattering, nuclear spallation, and Binary Cascade models for nucleon interactions below 10 GeV. The High Precision neutron transport module was activated to accurately model neutron elastic and inelastic scattering, radiative capture, and the $^{10}B(n,\alpha)^{7}Li$ capture reaction at all neutron energies, which is essential for correctly representing the boron-10 neutron capture contribution of the HBGPE layer. A global tracking cut of 1 micrometre was applied to suppress low-energy secondary electrons that do not contribute meaningfully to energy

deposition scoring while preserving accuracy for all primary particle types and energetically significant secondaries.

A total of 19 independent simulation runs were executed across three categories. The primary beam matrix comprised 12 runs spanning protons (10 MeV at 0°, 100 MeV at 0°, 1 GeV at 45°), electrons (0.1 MeV at 0°, 1 MeV at 45°, 10 MeV at 0°), gamma rays (0.1 MeV at 0°, 1 MeV at 45°), alpha particles (25 MeV/n at 0°, 250 MeV/n at 0°), and neutrons (1 MeV at 0°, 14 MeV at 0°), with the neutron runs selected to characterise the HBGPE boron-10 capture response across thermal and fast neutron energy ranges. An angular dependence study comprised four additional runs of 100 MeV protons at 15°, 30°, 45°, and 60° oblique incidence. Three aluminium comparison runs simulated identical beam configurations (100 MeV proton at 0°, 10 MeV electron at 0°, 1 MeV neutron at 0°) through a pure aluminium shield of equivalent total thickness (21.0 mm, six equal slices of 3.5 mm each) to provide direct performance benchmarking at identical total thickness. For oblique incidence runs, the primary particle source position was offset in the x-direction by the product of the source-to-shield distance and the tangent of the incidence angle, ensuring all oblique beams intercepted the shield centre. Primary particles were initiated at z = -5 cm upstream of the shield using a point source with zero angular spread. Each run simulated 1,000,000 primary events, for a total of 19,000,000 simulated primary events across all runs. Individual runs were specified via Geant4 macro files to ensure full reproducibility; all macro files and source code are provided in the Zenodo repository.

Energy deposition was scored on a per-event, per-layer basis using step-by-step tracking in the SteppingAction class. For each simulation step, total ionisation energy loss and nuclear recoil energy were accumulated per layer using the G4Step::GetTotalEnergyDeposit() method. Layer identification was performed by matching the current step's logical volume against the ordered vector of shield layer logical volumes registered at geometry construction. Primary particle transmission was scored per event: a primary particle was classified as transmitted if it exited the final Kapton layer boundary with positive z-direction momentum, evaluated at each geometry boundary crossing. All per-event data were written to comma-separated value (CSV) output files recording layer-wise energy deposition in MeV and the transmission flag. Per-run summary files recorded the mean and standard deviation of energy deposition per layer, transmission fraction, and attenuation fraction across all events. Statistical uncertainty in each result was estimated as the standard deviation of the per-event sample mean across 1,000,000 events per run. The Mersenne Twister pseudo-random number generator (CLHEP implementation) was used for all stochastic processes with fixed seed initialisation (seed: 12345) to ensure complete reproducibility of all reported simulation results.

Prototype electrical output testing

Electrical output characterisation was performed using a high-power heat gun (rated output 1,500 to 2,000 W) as a controlled infrared radiation source, providing consistent and repeatable thermal energy input to the shield surface at a fixed source-to-sample distance. This approach was adopted as a proof-

of-concept demonstration of the charge generation and transport capability of the conversion layer under controlled energy input conditions. Voltage and current output from the Kapton conduction layer were measured using a DT830D-type digital multimeter (voltage resolution 1 mV) connected via two conductive leads in a closed circuit configuration with output recorded across the measurement terminals. Power density was calculated as $P = V \times I / A$, where A represents the active sample area of 100 cm^2. Each flux condition was tested across five independent trials (n = 5), with measurements recorded manually and verified across repeated runs. Output variability was quantified as the percentage standard deviation relative to the mean for each condition. Energy transfer efficiency was calculated as the ratio of measured electrical energy output to estimated incident energy on the shield's outer (tungsten) surface, where incident energy was derived from the known rated output of the heat gun source and the exposed sample area. All efficiency values reported reflect IR-source test conditions specifically and do not represent particle radiation conversion efficiency.

Thermal testing

Thermal performance was evaluated using a butane/propane torch as the heat source. Sample surface temperature was monitored continuously using a handheld infrared pyrometer (maximum rated range 550 to 600°C) positioned at a consistent standoff distance from the sample surface throughout each test. Four thermal conditions were evaluated: sustained heating at 300°C for 10 minutes, sustained heating at 500°C for 4 minutes, direct torch flame exposure at 520°C for 8 seconds, and sustained direct torch flame exposure at 545°C for 1 minute. Peak surface temperatures of 520°C and 545°C represent the upper operating range of the pyrometer and should be interpreted accordingly. Surface temperature measurements reflect the outer tungsten layer surface and do not represent the temperature experienced by the inner HBGPE, scintillation, or graphene-PCL layers, which are expected to have been thermally buffered during short-duration exposures; characterisation of the thermal gradient across the full layer stack was not performed. Following each thermal exposure, samples were visually inspected for delamination, cracking, surface discolouration, and structural failure. Electrical output was re-measured after each condition to quantify output retention relative to the pre-test baseline. Five samples were tested at each condition (n = 5).

Mechanical testing

Compressive mechanical performance was evaluated by applying incremental loads of 20, 40, 60, 83, and 100 N to the sample surface using a controlled loading apparatus. Deformation was measured at each load level and recorded to two decimal places. Samples were visually and physically inspected after each loading increment for structural damage, layer separation, or deformation affecting functional layer integrity. Five samples were tested at each load level (n = 5). Drop impact testing was conducted by releasing a standardised impactor from fixed heights corresponding to impact energies of 5 J, 10 J, and 20 J, with samples assessed for visible surface damage and layer separation after each impact.

Areal density measurement

Areal density of the RADIANT shield was determined by direct mass measurement using a digital scale with a resolution of 0.01 g, with areal density calculated as measured sample mass divided by sample surface area (100 cm^2), yielding 48.27 $kg \cdot m^{-2}$. This value is consistent with the theoretical calculation from layer specifications of 47.61 $kg \cdot m^{-2}$, with the small difference of 0.66 $kg \cdot m^{-2}$ attributable to the mass contribution of the five interlayer epoxy bond lines not included in the theoretical estimate. The aluminium comparison shield areal density of 56.70 $kg \cdot m^{-2}$ was calculated from the product of the aluminium density (2.70 $g \cdot cm^{-3}$) and total shield thickness (21.0 mm), providing a direct mass comparison at identical total thickness. The RADIANT shield areal density of 48.27 $kg \cdot m^{-2}$ represents a 14.9% reduction relative to the equivalent-thickness aluminium reference.

Statistical analysis

All statistical analyses were performed using Microsoft Excel. Data are reported as mean plus or minus standard deviation (mean ± s.d.) unless otherwise stated. Prior to parametric testing, normality of all datasets was assessed using the Shapiro-Wilk test [14]; all datasets passed (electrical output: $W = 0.968$, $p = 0.312$; thermal retention: $W = 0.951$, $p = 0.381$; mechanical deformation: $W = 0.972$, $p = 0.512$). The relationship between incident flux and electrical power density was assessed using two-tailed linear regression ($n = 35$ total measurements across seven flux conditions). Differences in electrical output retention across thermal test conditions were assessed using one-way ANOVA, selected as appropriate for comparing a single independent variable (thermal condition) across four independent groups with normally distributed data ($F = 366.6$, $df = 3, 16$, $p < 0.001$). As only a single omnibus ANOVA was performed with no subsequent pairwise comparisons, no multiple comparison correction was required. Mechanical deformation as a function of applied load was assessed using two-tailed linear regression fitted to the five load-level means ($n = 5$ load conditions, slope = 0.0044 $mm \cdot N^{-1}$, $R^2 = 0.864$, $p = 0.022$); individual-trial-level regression was not performed as replicate-level deformation data were not pooled across load conditions for this analysis. The alpha level for all tests was set at 0.05. A sample size of $n = 5$ was selected based on prototype fabrication constraints and material availability; the low power of the Shapiro-Wilk test to detect non-normality at $n = 5$ is acknowledged as a limitation of the normality assessment [14]. No radioactive materials were used in this study. All experimental testing was conducted using commercial infrared and thermal sources, and no radiation safety licensing or institutional ethics approval was required for the experimental procedures described. The scientific content and manuscript preparation were entirely the work of the author. All concepts, study design, methodology, simulations, source code, experimental data, analyses, scientific interpretations, figures, tables, and conclusions are solely the work of the author. An AI language model (Claude, Anthropic) was used solely for minimal language editing to improve grammar, clarity, and readability. All raw data, Geant4 source code, simulation macro files, and output data files are available in the repository listed in the Data Availability Statement.

Declarations

Competing interests

The author declares no competing interests.a

Funding

This research received no external funding.

Author Contribution

K.D.P. conceived the study, designed and fabricated the prototype, conducted all experiments, performed data analysis and statistical testing, wrote all simulation code, executed all 19 Geant4 particle transport simulation runs, and wrote the manuscript in its entirety.

Acknowledgement

The author thanks Mr. Kevin Cardoso and Mr. Hamed Shateri for guidance on experimental design and scientific rigour. Laboratory facilities and equipment were provided by the Science Department, Milliken Mills High School.

Data Availability

All raw experimental data, Geant4 simulation input files and output data, simulation spreadsheet models, and statistical analysis files generated and used during this study are publicly available in the Zenodo repository at https://doi.org/10.5281/zenodo.21459473. All Geant4 11.2.2 simulation source code (C++ classes and CMake build files) and macro files for all 19 simulation runs are also available in the same repository, alongside the per-event and per-run summary output CSV files. All materials are provided under a CC BY 4.0 licence. Any additional data or code are available from the corresponding author upon reasonable request.

Code availability

All Geant4 11.2.2 simulation source code (C + + classes and CMake build files) and macro files for all 19 simulation runs are available in the Zenodo repository at https://doi.org/10.5281/zenodo.21459473, alongside the per-event and per-run summary output CSV files. Code is provided under a CC BY 4.0 licence.

References

1. Wertz, J. R., Everett, D. F. & Puschell, J. J. (eds) *Space Mission Engineering: The New SMAD* (Microcosm, 2011).
2. Wilson, J. W. et al. NASA,. Transport methods and interactions for space radiations. NASA Reference Publication 1257 (1991).
3. Simpson, J. A. Elemental and isotopic composition of the galactic cosmic rays. *Annu. Rev. Nucl. Part. Sci.* **33**, 323–381 (1983).
4. Naito, M. et al. Investigation of shielding material properties for effective space radiation protection. *Life Sci. Space Res.* **26**, 69–76 (2020).
5. Barthel, J. Sarigul-Klijn, N. A review of radiation shielding needs and concepts for space voyages beyond Earth's magnetic influence. *Prog Aerosp. Sci.* **110**, 100553 (2019).
6. Singh, P., Dosovitskiy, G. & Bekenstein, Y. Bright innovations: review of next-generation advances in scintillator engineering. *ACS Nano*. **18**, 14029–14049 (2024).
7. Hofstadter, R. Alkali halide scintillation counters. *Phys. Rev.* **74**, 100–104 (1948).
8. Sahi, S., Chen, W. & Jiang, K. Luminescence enhancement of PPO/PVT scintillators by CeF3 nanoparticles. *J. Lumin.* **159**, 105–109 (2015).
9. DuPont DuPont,. Kapton HN polyimide film: summary of properties. (2023). https://www.dupont.com/products/kapton-hn.html
10. Archer, E., Torretti, M. & Madbouly, S. Biodegradable polycaprolactone (PCL) based polymer and composites. *Phys. Sci. Rev.* **8**, 4391–4414 (2023).
11. Nambiar, S. & Yeow, J. T. W. Polymer-composite materials for radiation protection. *ACS Appl. Mater. Interfaces*. **4**, 5717–5726 (2012).
12. Inuwa, I. M. et al. Graphene nanocomposites in space sector: fundamentals and advancements. *C* **9**, 29 (2023).
13. Agostinelli, S. et al. Geant4: a simulation toolkit. *Nucl. Instrum. Methods Phys. Res. A*. **506**, 250–303 (2003).
14. Shapiro, S. S. & Wilk, M. B. An analysis of variance test for normality (complete samples). *Biometrika* **52**, 591–611 (1965).
15. Navarro, R., Burillo, G., Adem, E. & Marcos-Fernández, A. Effect of ionizing radiation on the chemical structure and the physical properties of polycaprolactones of different molecular weight. *Polymers* **10**, 397 (2018).

Figures

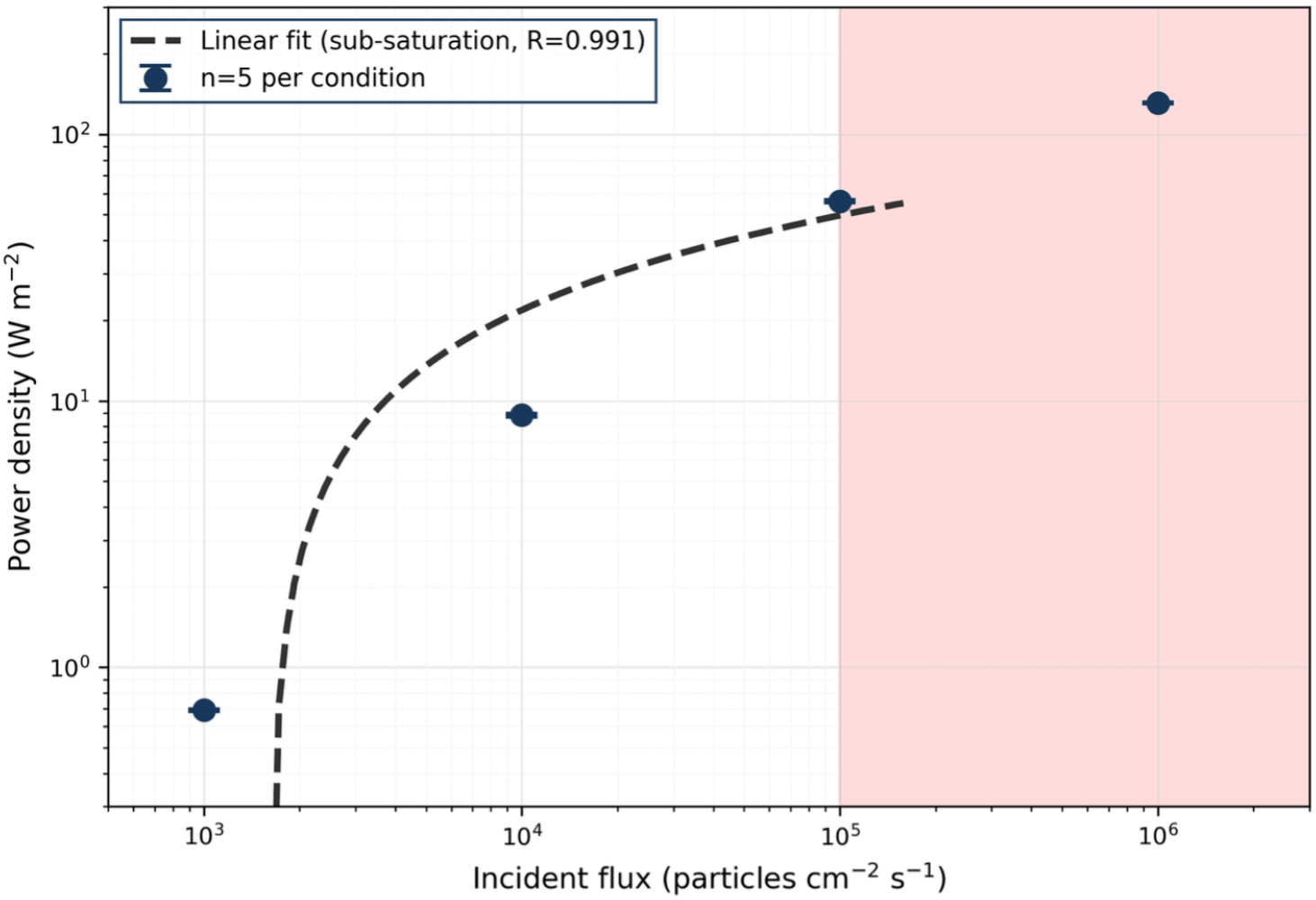


Figure 1

Electrical output as a function of incident energy flux. Mean power density (W·m⁻²) plotted against incident flux (particles·cm⁻²·s⁻¹) for n = 5 prototype samples per condition. Error bars represent s.d. Output increased from 0.69 ± 0.007 W·m⁻² at the lowest flux condition to 131.05 ± 0.47 W·m⁻² at the highest, with variability below ±1.04% across all trials. The dashed line shows a linear regression fit applied to the sub-saturation regime ($p < 0.001$, $R^2 = 0.991$, two-tailed); the shaded region marks the two highest flux conditions, which deviate from this fit, consistent with saturation of available excited states in the cerium-doped scintillation centres at high incident flux. Both axes are logarithmic. Electrical output was characterised using a controlled infrared radiation source as a proof-of-concept energy input; higher flux conditions were informed by simulation modelling of space radiation environments.

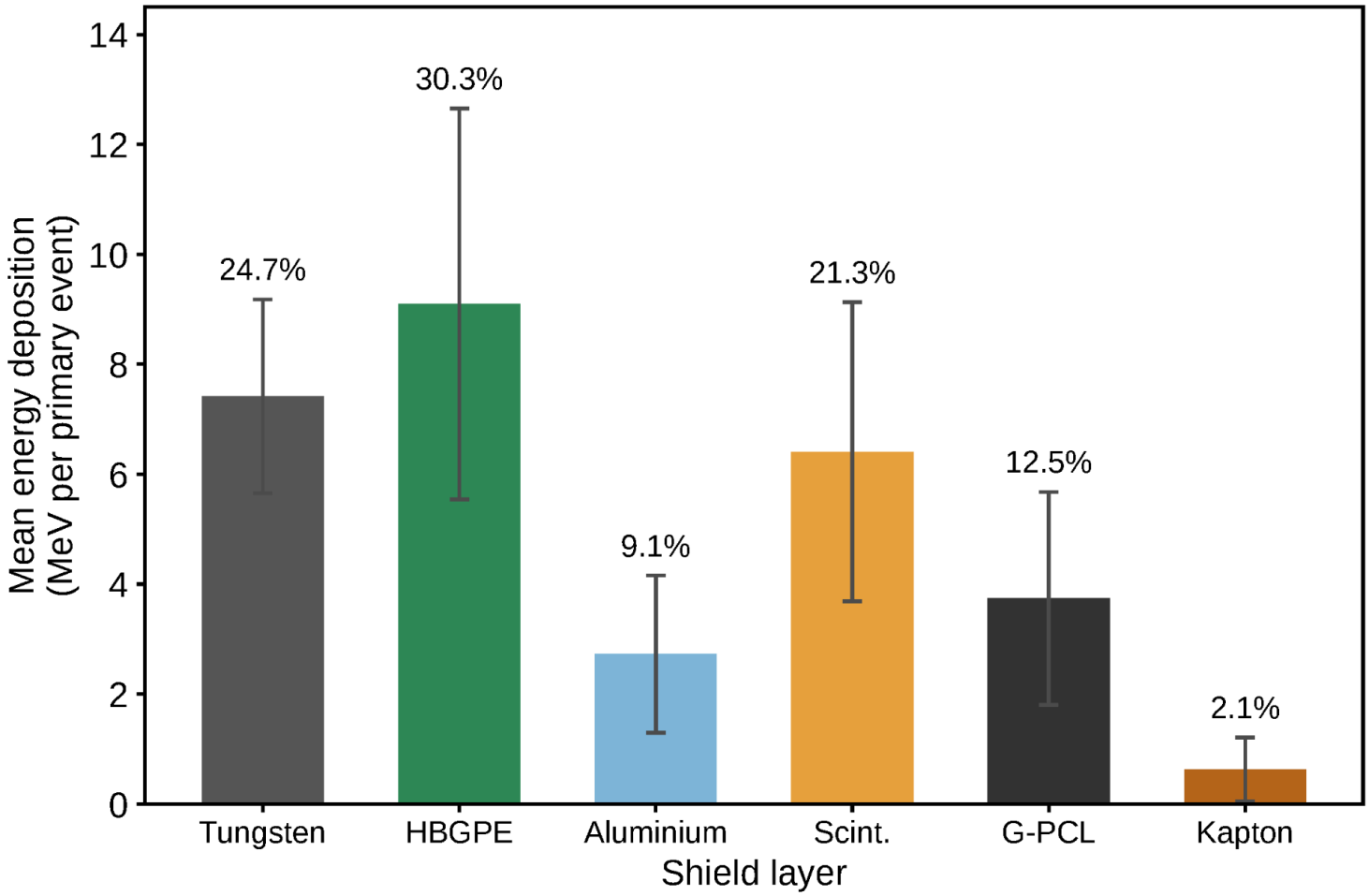


Figure 2

Geant4-simulated energy deposition across shield layers. Mean energy deposition (MeV per primary event) per shield layer from the 100 MeV proton simulation run (P2), based on Geant4 11.2.2 particle transport simulation [13] with 1,000,000 primary events. Percentage values above each bar indicate the fraction of total deposited energy absorbed by that layer. Error bars represent s.d. of per-event energy deposition across the 1,000,000 simulated primary events (not the standard error of the mean), reflecting event-to-event variability rather than uncertainty in the reported mean. Layers shown from outermost to innermost: tungsten initial capture layer (Tungsten), HBGPE composite primary stopping layer (HBGPE), aluminium structural interlayer (Aluminium), cerium-doped scintillation layer (Scint.), graphene-PCL charge collection layer (G-PCL), and Kapton HN conduction layer (Kapton). The HBGPE layer received the highest fractional energy deposition (30.3%), with the scintillation layer receiving 21.3% of total deposited energy. Physics list: QGSP_BIC_HP.

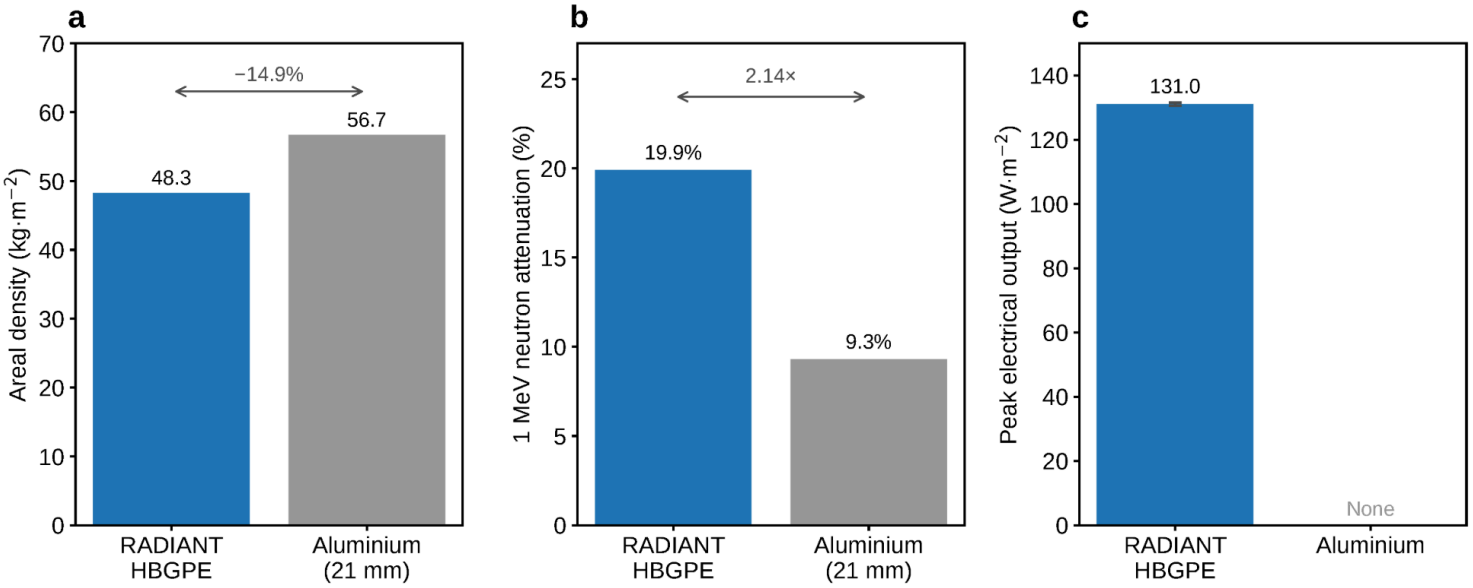


Figure 3

System-level comparison of RADIANT HBGPE shield and equivalent-thickness aluminium shielding. Three performance metrics compared side by side for RADIANT (blue) and conventional aluminium shielding (grey), both at 21.0 mm total thickness. **a**, Areal density (kg·m⁻²); RADIANT value determined by direct mass and surface area measurement (48.27 kg·m⁻²), aluminium reference calculated from material density and equivalent thickness (56.70 kg·m⁻²); RADIANT is 14.9% lighter. No error bars are applicable; both values represent single direct measurements or calculations rather than replicate trials. **b**, 1 MeV neutron attenuation (%); RADIANT achieves 2.14× higher neutron attenuation than aluminium at equivalent thickness. Statistical (counting) uncertainty, based on N = 1,000,000 primary events per run, is <0.1% and smaller than the plotted symbols; error bars are omitted accordingly. **c**, Peak electrical output (W·m⁻²) under IR energy input at the highest tested flux condition (n = 5); error bars represent s.d.; the aluminium reference produced no measurable output.

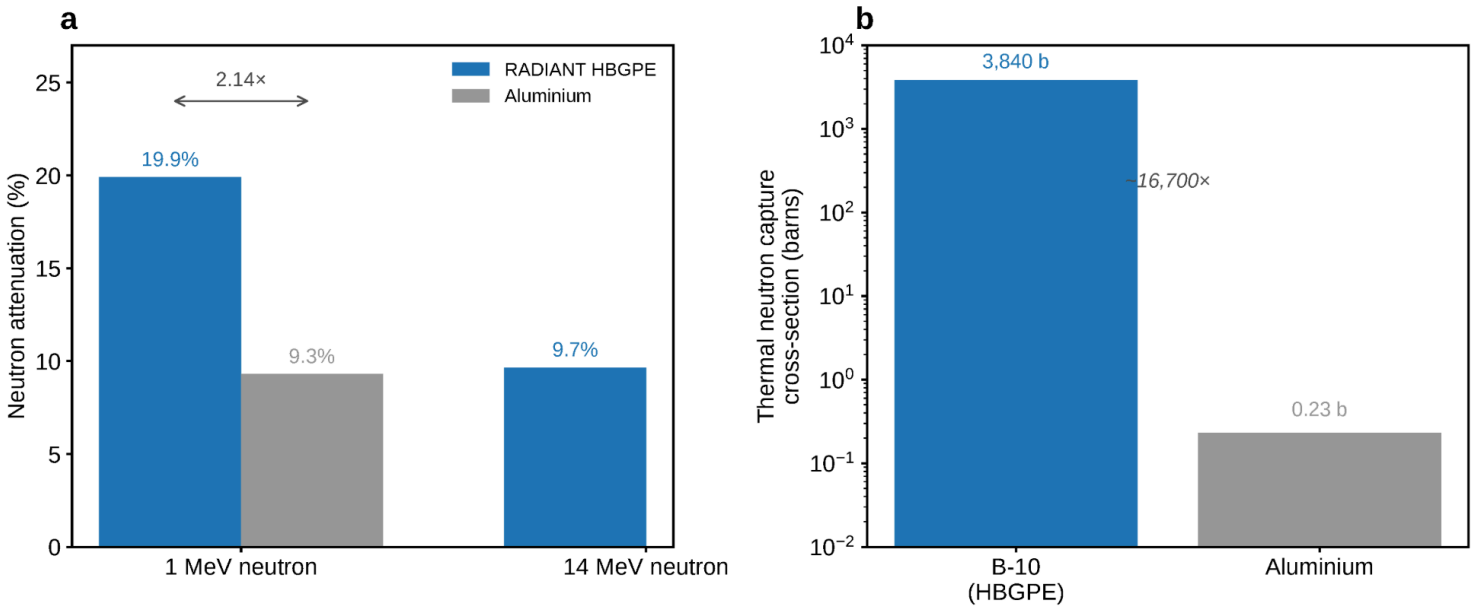


Figure 4

Neutron attenuation performance and boron-10 capture cross-section advantage. **a**, Neutron attenuation percentage for the RADIANT HBGPE shield and equivalent-thickness aluminium shield at 1 MeV and 14 MeV neutron energies, based on Geant4 11.2.2 simulation [13] with 1,000,000 primary events per run; RADIANT achieves 2.14× higher attenuation than aluminium at 1 MeV (19.90% versus 9.30%). Statistical (counting) uncertainty, based on N = 1,000,000 primary events per run, is <0.1% and smaller than the plotted symbols; error bars are omitted accordingly. No aluminium comparison run was conducted at 14 MeV. **b**, Thermal neutron capture cross-section (barns, logarithmic scale) for enriched boron-10 (3,840 barns, modelled in the HBGPE composite Geant4 simulation at 25% mass fraction with 95% ^{10}B isotopic abundance as a design optimisation scenario) and aluminium (0.23 barns), illustrating the approximately 16,700-fold cross-section advantage of the B-10 component. Values are literature reference cross-sections, not experimental or simulated measurements; error bars are not applicable. Physics list: QGSP_BIC_HP with high-precision neutron transport.

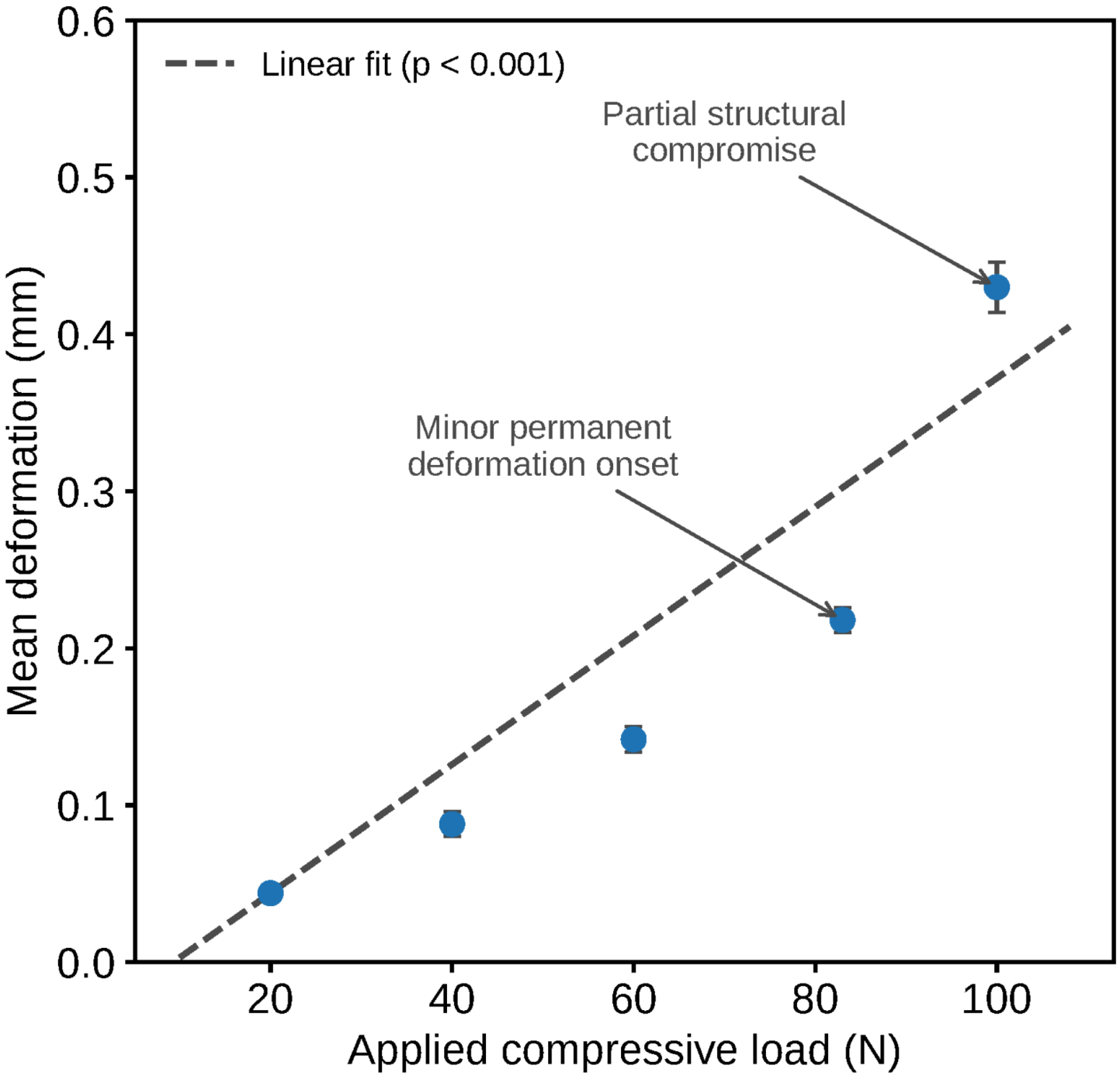


Figure 5

Mechanical deformation as a function of applied compressive load. Mean deformation (mm) plotted against applied load (N) for n = 5 samples per load level. Error bars represent s.d. The dashed line shows a linear regression fit across the full load range ($p < 0.001$, $R^2 = 0.864$, slope = 0.0044 mm·N^{-1}, two-tailed). The onset of minor permanent deformation was recorded at 83 N and partial structural compromise at 100 N, as annotated. No complete fracture or full delamination occurred at any load level tested.

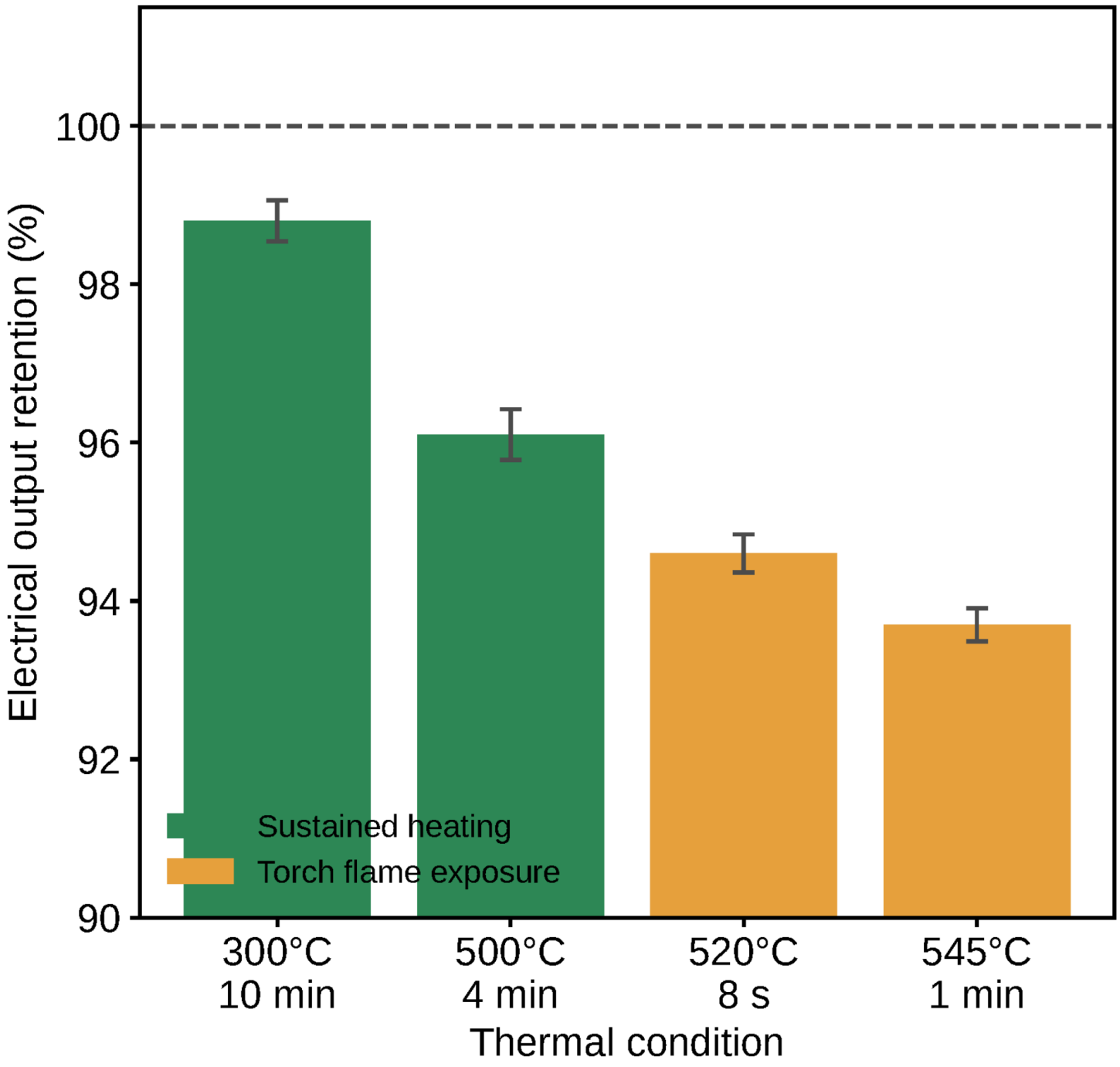


Figure 6

Electrical output retention across thermal test conditions. Mean output retention (%) relative to pre-test baseline for n = 5 samples at each thermal condition. Error bars represent s.d. Teal bars represent sustained heating conditions (300°C for 10 minutes; 500°C for 4 minutes). Amber bars represent direct torch flame exposure conditions (520°C for 8 seconds; 545°C for 1 minute). The dashed line at 100% indicates the pre-test baseline. Peak surface temperatures were recorded by handheld infrared pyrometer (maximum rated range: 550 to 600°C) on the outer tungsten surface. One-way ANOVA confirmed statistically significant differences in output retention across conditions ($F = 366.6$, $df = 3, 16$, $p < 0.001$); all values remained above 93%.

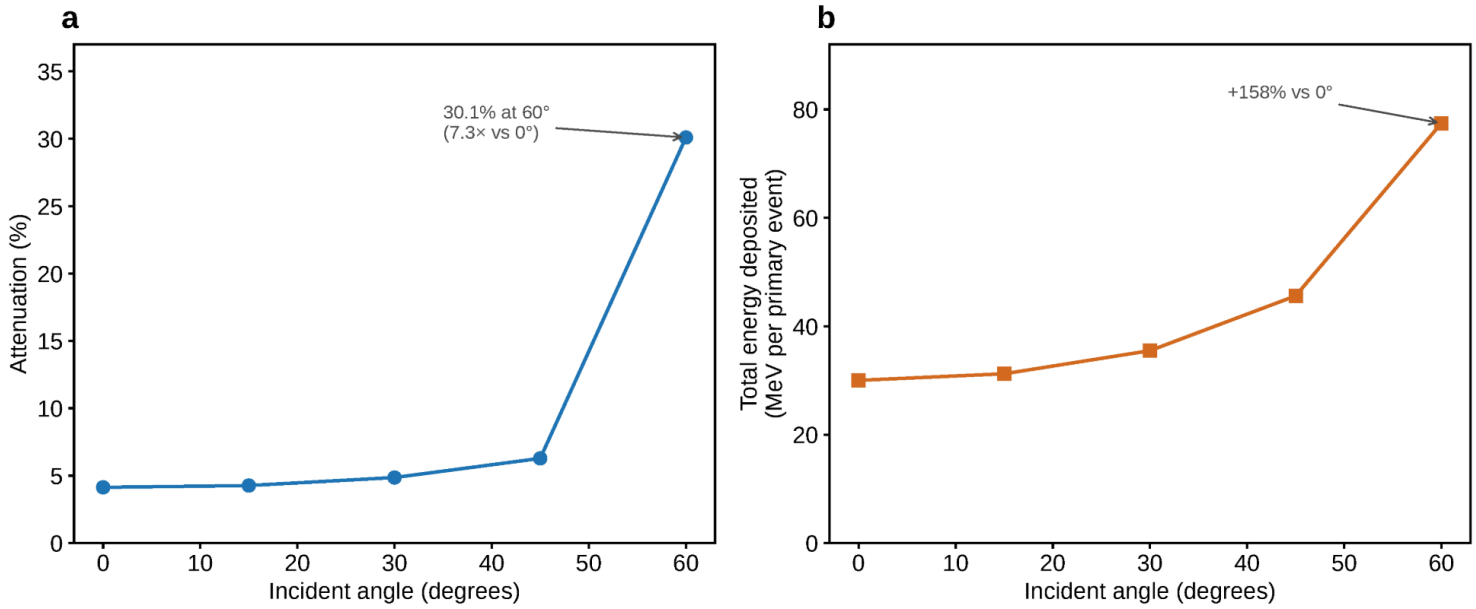


Figure 7

Angular dependence of radiation attenuation and energy deposition for 100 MeV protons. **a**, Attenuation percentage at oblique incidence angles from 0° to 60°. **b**, Total mean energy deposited per primary event (MeV) at each angle. Both panels are based on Geant4 11.2.2 particle transport simulation [13] with 1,000,000 primary events per run, QGSP_BIC_HP physics list. Statistical (counting) uncertainty, based on N = 1,000,000 primary events per run, is <0.1% and smaller than the plotted symbols; error bars are omitted accordingly. Attenuation increased from 4.13% at normal incidence to 30.09% at 60°, a 7.3-fold improvement. Total energy deposited increased by 158% between 0° and 60°, consistent with the increased effective path length through the shield stack at oblique angles.

Supplementary Files

This is a list of supplementary files associated with this preprint. Click to download.

- SupplementaryTableS1.pdf
- SupplementaryTableS2.pdf